GEOPHYSICS, VOL. 88, NO. 1 (JANUARY-FEBRUARY 2023); P. MR25–MR33, 10 FIGS., 2 TABLES.
10.1190/GEO2021-0815.1

Check for updates

Downloaded 11/13/23 to 140.105.71.236. Redistribution subject to SEG license or copyright; see Terms of Use at http://library.seg.org/page/policies/terms
DOI:10.1190/geo2021-0815.1

Amplitude-variation-with-offset in thermoelastic media

Wanting Hou[1], Li-Yun Fu[2], and José M. Carcione[3]

ABSTRACT

Temperature is an important factor for evaluating the seismic response of deep reservoirs. We have developed an amplitude-variation-with-offset approximation based on the Lord-Shulman thermoelasticity theory. The model predicts two compressional (P and T) waves (the second is a thermal mode) and a shear (S) wave. The T mode is due to the coupling between the elastic and heat equations. In the thermoelastic case, the approximation is more accurate than in the elastic case. Its accuracy is verified by comparison with the exact equations calculated in terms of potential functions. We examine two reservoir models with high temperatures and compute synthetic seismograms that illustrate the reliability of the approximation. Moreover, we consider real data to build a model and find that the approximate equation not only simplifies the calculations but also is accurate enough and can be used to evaluate the temperature-dependent elastic properties, providing a basis for further application of the thermoelasticity theory, such as geothermal exploration, thermal-enhanced oil recovery, and ultradeep oil and gas resources subject to high temperatures.

INTRODUCTION

Amplitude-variation-with-offset (AVO) analysis is an important method in seismic exploration, extensively used to estimate the properties of reservoirs. As petroleum exploration of deep resources develops, the emphasis is increasingly on high-pressure high-temperature reservoirs. Thermoelasticity, which couples the elastic and heat equations, can be applied in this situation; specifically, the theory couples the fields of deformation and temperature. We investigate the application of AVO including the thermal effects — absent in the classical theory of elasticity — to the seismic response of reservoirs. The effects of the thermal properties on wave velocity and attenuation characteristics have been investigated by Hou et al. (2021a).

The conventional coupled theory of thermoelasticity is established based on the Fourier law of heat conduction (Biot, 1956a; Deresiewicz, 1957), leading to discontinuities and infinite velocities due to a parabolic-type heat equation. Lord and Shulman (1967) introduce a relaxation term in this equation to overcome this problem. It can be seen as an analogy to Maxwell's model of viscoelasticity (Maxwell, 1867; Carcione et al., 2019). Furthermore, besides the fast P and S waves, the theory predicts an additional one called the thermal wave (or T wave), whose behavior is similar to the slow P wave of poroelasticity (Biot, 1956b). The existence of this wave has been proven by experimental measurements in solid helium (Ackerman et al., 1966) and sodium fluoride (NaF) crystals (Jackson et al., 1970; McNelly et al., 1970) and has been simulated by analytical (Wang et al., 2020b; Wei et al., 2020) and numerical methods (Carcione et al., 2019; Hou et al., 2021b).

Abbas and Othman (2012) consider a thermoelastic solid half-space to study the behavior of wave propagation based on the Lord-Shulman (LS) theory. A generalization of the LS theory with more relaxation times has been proposed by Green and Lindsay (1972) (Green-Lindsay [GL] theory). Sinha and Elsibai (1996) and Zenkour et al. (2013) study the reflection of thermoelastic waves at a free surface by using the GL theory. Research on reflection and refraction phenomena at a liquid-solid interface has been performed by Singh (2000), who compares the LS, GL, and isothermal cases. The results show that the thermal effects are nonnegligible. More recently, Sarkar and Mondal (2020) consider a stress-free and thermally insulated surface analyzed with a modified GL theory. However, these authors ignore the presence of inhomogeneous (body) plane waves, thus violating the Snell law. On the other hand,

Manuscript received by the Editor 21 December 2021; revised manuscript received 18 September 2022; published ahead of production 31 October 2022; published online 6 January 2023.
[1]China University of Petroleum (East China), Key Laboratory of Deep Oil and Gas, Qingdao, China. E-mail: hwtupc@163.com.
[2]China University of Petroleum (East China), Key Laboratory of Deep Oil and Gas, Qingdao, China and Qingdao National Laboratory for Marine Science and Technology, Laboratory for Marine Mineral Resources, Qingdao, China. E-mail: lfu@upc.edu.cn (corresponding author).
[3]National Institute of Oceanography and Applied Geophysics — INOGS, Trieste, Italy and Hohai University, Nanjing, China. E-mail: jose.carcione@gmail.com.
© 2023 Society of Exploration Geophysicists. All rights reserved.

Downloaded 11/13/23 to 140.105.71.236. Redistribution subject to SEG license or copyright; see Terms of Use at http://library.seg.org/page/policies/terms
DOI:10.1190/geo2021-0815.1

Sharma (2018) and Wang et al. (2021), by using the theory of thermo-poroelasticity, consider the inhomogeneous waves to study the scattering (reflection and transmission [R/T]) coefficients.

The R/T coefficients provide a basis for AVO in reflection seismology. Their variations with the incidence and azimuth angles contain valuable information of the subsurface, such as wave velocities, elastic stiffness, and fluid content. Zoeppritz (1919) derives analytical expressions for the plane-wave scattering coefficients using welded boundary conditions at an interface between two elastic half-spaces. Because the expressions are cumbersome to implement in AVO, many geophysicists have developed approximations, namely, Koefoed (1955) and Shuey (1985) propose expressions in terms of the Poisson ratio and S-wave velocity, respectively (Bortfeld, 1961; Aki and Richards, 2002).

Viscoelasticity has been introduced in the AVO theory with the concept of quality factor (e.g., Carcione, 1995, 1997). Shen and Wang (2013) derive an approximation for viscoelastic media in which the quality factor and inhomogeneity angle are regarded as perturbations. For poroelasticity, Chapman et al. (2006) consider the fluid sensitivity of AVO analysis based on the squirt-flow model, and the effect of mobility has been further studied (Zhao et al., 2017). Zong et al. (2012) obtain approximate expressions of the coefficients focusing on the extraction of the fluid term in porous media. Velocity dispersion and attenuation are highly sensitive to pressure and temperature (Batzle et al., 2006). In this work, we propose a novel AVO equation based on the thermoelasticity theory and the linearized Aki-Richards approximation (Aki and Richards, 2002) as in Zong et al. (2012). The exact R/T coefficients based on the LS theory are calculated by considering the generalized Snell law and verified by conservation of energy, in which wave inhomogeneity is honored. Then, we obtain an AVO approximation, including the thermal properties, verified by the exact coefficients and compute synthetic seismograms that illustrate the reliability of the approximation. Finally, we consider a real-data example.

THERMOELASTICITY

LS theory

Lord and Shulman (1967) obtain a hyperbolic heat equation with a relaxation time τ generalizing Biot (1956a):

$$\beta T_0 \dot{u}_{j,j} + c\dot{T} + \tau(c\ddot{T} + \beta T_0 \ddot{u}_{j,j}) = \bar{\gamma} T_{,jj}, \tag{1}$$

where u_j ($j = x, y, z$) is the components of the displacement field; T is the increment of temperature above a reference absolute temperature T_0 for the state of zero stress and strain; c and $\bar{\gamma}$ are the specific heat of the unit volume in the absence of deformation and the coefficient of heat conduction, respectively; the Einstein implicit summation is used; and a dot above a variable represents time (t) differentiation. The compressional stiffness per unit temperature or elastic/heat coupling coefficient is

$$\beta = (3\lambda + 2\mu)\bar{\alpha}, \tag{2}$$

where λ and μ are the Lamé constants and $\bar{\alpha}$ is the linear coefficient of thermal expansion.

In isotropic media, the elastic equation with the thermal coupling term is

$$(\lambda + \mu)u_{j,ji} + \mu u_{i,jj} - \beta T_{,i} - \rho \ddot{u}_i = 0, \tag{3}$$

where ρ is the material density. See Carcione et al. (2019).

Plane-wave analysis

Introducing the Helmholtz decomposition of the scalar potential ϕ and vector potential $\psi\hat{\mathbf{n}}$ (or $\boldsymbol{\psi}$), the displacement vector is

$$\mathbf{u} = \nabla\phi + \nabla \times \psi\hat{\mathbf{n}}. \tag{4}$$

Following Carcione (2014) and the notations of Wang et al. (2021), we consider the plane-wave solution:

$$\mathbf{U} = \mathbf{A}\ \exp[\mathrm{i}(\omega t - \mathbf{k}\cdot\mathbf{x})], \tag{5}$$

where $\mathbf{U} = [T, \phi, \psi]$, $\mathbf{A} = [A_T, A_\phi, A_\psi]$ is the amplitude vector, $\mathbf{x} = [x, y, z]$ is the position vector, $\mathbf{k}$ is the complex wavenumber vector, ω is the angular frequency, and $\mathrm{i} = \sqrt{-1}$. We have

$$\mathbf{k} = \kappa\hat{\boldsymbol{\kappa}} - \mathrm{i}\alpha\hat{\boldsymbol{\alpha}}, \tag{6}$$

where the real and imaginary parts correspond to the real wavenumber and attenuation vectors, respectively, whose directions for the inhomogeneity angle γ. When $\hat{\boldsymbol{\kappa}}$ and $\hat{\boldsymbol{\alpha}}$ coincide ($\gamma = \hat{0}$), the waves are homogeneous. We consider the general inhomogeneous case and obtain from Appendix A (equation A-2)

$$\left[a_0 V_0^2, -\left(a_0 + V_0^2 + \frac{\beta^2}{\rho c} T_0\right)\omega^2, \omega^4\right] \cdot \begin{bmatrix} k^4 \\ k^2 \\ 1 \end{bmatrix} = 0, \tag{7}$$

where

$$a_0 = \frac{\mathrm{i}\omega\bar{\gamma}}{c(1 + \mathrm{i}\tau\omega)}, \quad V_0^2 = \frac{\lambda + 2\mu}{\rho}. \tag{8}$$

This equation can be solved for the square of the wavenumber (k^2) giving two solutions related to the P and T waves. Note that k^2 is independent of γ because it is a material property, but according to Borcherdt (2009, equations 3.1.20 and 3.1.21) and Carcione (2014, equation 3.34), κ and α depend on γ.

The phase velocities (V) and attenuation factors (A) of homogeneous (subscript H) and inhomogeneous (subscript In) waves are defined, respectively, as (Borcherdt, 2009; Carcione 2014)

$$V_{\mathrm{H}} = \left[\mathrm{Re}\left(\frac{1}{V_{\mathrm{c}}}\right)\right]^{-1}, \quad A_{\mathrm{H}} = -\omega\mathrm{Im}\left(\frac{1}{V_{\mathrm{c}}}\right), \quad V_{\mathrm{c}} = \frac{\omega}{k},$$
$$V_{\mathrm{In}} = \frac{\omega}{\kappa}, \qquad A_{\mathrm{In}} = \alpha. \tag{9}$$

Similarly, the phase velocity of the S wave is (Hou et al., 2022)

$$V_{\mathrm{S}} = \sqrt{\frac{\mu}{\rho}}. \tag{10}$$

Deresiewicz (1957) proposes an alternative attenuation coefficient L:

Downloaded 11/13/23 to 140.105.71.236. Redistribution subject to SEG license or copyright; see Terms of Use at http://library.seg.org/page/policies/terms
DOI:10.1190/geo2021-0815.1

$$L = 4\pi \frac{A \cdot V}{\omega}. \tag{11}$$

R/T COEFFICIENTS

Zoeppritz equations

We consider a 2D plane interface ($z = 0$). The boundary conditions at the interface between two thermoelastic media Ω_{I} ($z > 0$) and Ω_{II} ($z < 0$) are the continuity of the normal and tangential displacements and stresses, temperature, and heat flux (e.g., Ignaczak and Ostoja-Starzewski, 2010):

$$u_z^{\mathrm{I}} = u_z^{\mathrm{II}}, \quad u_x^{\mathrm{I}} = u_x^{\mathrm{II}}, \quad \sigma_{zz}^{\mathrm{I}} = \sigma_{zz}^{\mathrm{II}}, \quad \sigma_{xz}^{\mathrm{I}} = \sigma_{xz}^{\mathrm{II}},$$
$$T^{\mathrm{I}} = T^{\mathrm{II}}, \quad \bar{\gamma}^{\mathrm{I}} \frac{\partial T^{\mathrm{I}}}{\partial z} = \bar{\gamma}^{\mathrm{II}} \frac{\partial T^{\mathrm{II}}}{\partial z}, \tag{12}$$

where the superscripts I and II refer to the incidence and transmission media, respectively. An inhomogeneous plane wave incident obliquely in Ω_{I} generates three reflected waves in Ω_{I} (P, T, and S waves) and three transmitted waves in Ω_{II}.

For an incident P wave, the potential functions are

$$\phi^{\mathrm{I}} = A_0 \exp[\mathrm{i}(\omega t - p_0 x + q_0 z)] + \sum_{m=1}^{2} (A_m \exp[\mathrm{i}(\omega t - p_m x - q_m z)]),$$
$$\psi^{\mathrm{I}} = A_3 \exp[\mathrm{i}(\omega t - p_3 x - q_3 z)],$$
$$\phi^{\mathrm{II}} = \sum_{m=4}^{5} (A_m \exp[\mathrm{i}(\omega t - p_m x + q_m z)]),$$
$$\psi^{\mathrm{II}} = A_6 \exp[\mathrm{i}(\omega t - p_6 x + q_6 z)], \tag{13}$$

where the subscript 0 refers to the incident wave; the reflected P, T, and S waves have subscripts 1, 2, and 3, respectively; and the transmitted P, T, and S waves have subscripts 4, 5, and 6, respectively, which also identify other properties, e.g., wavenumbers, R/T coefficients, and phase angles.

For an incident S wave, we have

$$\phi^{\mathrm{I}} = \sum_{m=1}^{2} (A_m \exp[\mathrm{i}(\omega t - p_m x - q_m z)]),$$
$$\psi^{\mathrm{I}} = A_0 \exp[\mathrm{i}(\omega t - p_0 x + q_0 z)] + A_3 \exp[\mathrm{i}(\omega t - p_3 x - q_3 z)], \tag{14}$$

(the potential functions of the transmitted waves in Ω_{II} are similar to those of the incident P wave). In these equations, p_m are the horizontal wavenumbers given by Wang et al. (2020a, 2021):

$$p_0 = p_m = |\kappa_0| \sin\theta_0 - \mathrm{i}|\alpha_0| \sin(\theta_0 - \gamma_0), \quad m = 1, 2 \ldots 6, \tag{15}$$

where $|\kappa_0|$ and $|\alpha_0|$ are the magnitudes of the incident wave propagation and attenuation vectors in equation 6, respectively; θ is the angle between the interface normal and the direction of propagation; and γ is the angle between the directions of propagation ($\hat{\boldsymbol{\kappa}}$) and attenuation ($\hat{\boldsymbol{\alpha}}$) shown in Figure 1. The vertical wavenumbers q_m can be obtained as

$$q_m = d_m^{\mathrm{R}} + \mathrm{i} d_m^{\mathrm{I}}, \; d_m = \mathrm{PV}\sqrt{k_m^2 - p_m^2}, \; m = 0, 1 \ldots 6, \tag{16}$$

where PV takes the principal value of the complex quantity d_m, whose real and imaginary parts are denoted by d_m^{R} and d_m^{I}, respectively.

Substituting the potential functions 13 or 14 into equations 1 and 3 and considering the boundary conditions (equation 12), we obtain the Zoeppritz equations of the thermoelasticity theory:

$$\mathbf{B} \cdot \mathbf{R} = \mathbf{D}, \tag{17}$$

where matrices $\mathbf{B}$ and $\mathbf{D}$ are given in Appendix B for an incident P wave and the components of the amplitude ratio $\mathbf{R}$ (a 6×1 matrix) are

$$R_{m1} = R_m^{\mathrm{R}} = \frac{A_m}{A_0},$$
$$C_{m1} = C_m^{\mathrm{R}} = R_m^{\mathrm{R}} \frac{k_m}{k_0} = |C_m^{\mathrm{R}}| \exp(\mathrm{i}\vartheta_m), \quad m = 1, 2, 3,$$
$$R_{n1} = R_n^{\mathrm{T}} = \frac{A_n}{A_0},$$
$$C_{n1} = C_n^{\mathrm{T}} = R_n^{\mathrm{T}} \frac{k_n}{k_0} = |C_n^{\mathrm{T}}| \exp(\mathrm{i}\vartheta_n), \quad n = 4, 5, 6, \tag{18}$$

where the meaning of subscripts m and n is similar to those of equation 13; C represents the 6×1 matrix of R/T coefficients defined by $\mathbf{R}$; the superscripts R and T refer to reflection and transmission, respectively; $|C_m^{\mathrm{R}}|(|C_n^{\mathrm{T}}|)$ represents the magnitude of the complex quantity $C_m^{\mathrm{R}}(C_n^{\mathrm{T}})$; and $\vartheta_m(\vartheta_n)$ represents the corresponding phase angles.

AVO approximation

Under the assumption that only small relative changes in elastic properties occur across the interface of two welded solid half-spaces, the P- and S-wave R/T coefficients in terms of the perturbations of the velocities and density (ΔV_{S} and $\Delta\rho$) are

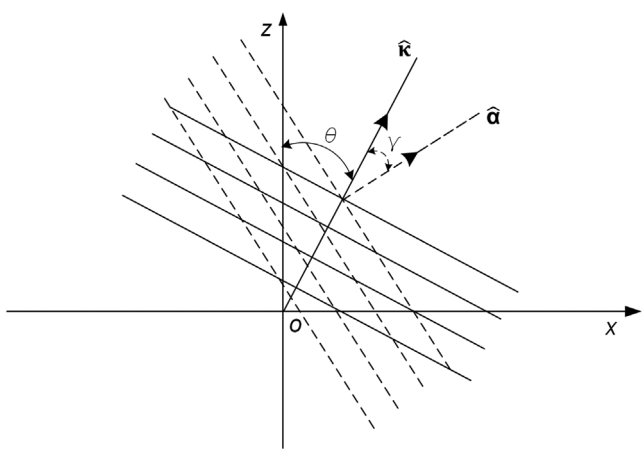

Figure 1. Inhomogeneous thermoelastic plane wave. The propagation angle θ and inhomogeneity angle γ.

Downloaded 11/13/23 to 140.105.71.236. Redistribution subject to SEG license or copyright; see Terms of Use at http://library.seg.org/page/policies/terms
DOI:10.1190/geo2021-0815.1

$$
\begin{aligned}
(R_{\mathrm{PP}})_{\mathrm{H}} &= \left[\frac{1}{2} - 2\sin^2\theta\left(\frac{V_{\mathrm{S}}}{V_{\mathrm{H}}}\right)^2\right]\frac{\Delta\rho}{\rho} \\
&\quad + \frac{1}{\cos^2\theta}\frac{\mathrm{Re}(k^{\mathrm{I}}) - \mathrm{Re}(k^{\mathrm{II}})}{\mathrm{Re}(k^{\mathrm{I}}) + \mathrm{Re}(k^{\mathrm{II}})} - 4\sin^2\theta\left(\frac{V_{\mathrm{S}}}{V_{\mathrm{H}}}\right)^2\frac{\Delta V_{\mathrm{S}}}{V_{\mathrm{S}}}, \\
(R_{\mathrm{PP}})_{\mathrm{In}} &= \left[\frac{1}{2} - 2\sin^2\theta\left(\frac{V_{\mathrm{S}}}{V_{\mathrm{In}}}\right)^2\right]\frac{\Delta\rho}{\rho} \\
&\quad + \frac{1}{\cos^2\theta}\frac{\kappa^{\mathrm{I}} - \kappa^{\mathrm{II}}}{\kappa^{\mathrm{I}} + \kappa^{\mathrm{II}}} - 4\sin^2\theta\left(\frac{V_{\mathrm{S}}}{V_{\mathrm{In}}}\right)^2\frac{\Delta V_{\mathrm{S}}}{V_{\mathrm{S}}}, \\
(T_{\mathrm{PP}})_{\mathrm{H}} &= 1 - \frac{1}{2}\frac{\Delta\rho}{\rho} + \left(\frac{1}{2\cos^2\theta} - 1\right)\frac{\mathrm{Re}(k^{\mathrm{I}}) - \mathrm{Re}(k^{\mathrm{II}})}{\mathrm{Re}(k^{\mathrm{I}}) + \mathrm{Re}(k^{\mathrm{II}})}, \\
(T_{\mathrm{PP}})_{\mathrm{In}} &= 1 - \frac{1}{2}\frac{\Delta\rho}{\rho} + \left(\frac{1}{2\cos^2\theta} - 1\right)\frac{\kappa^{\mathrm{I}} - \kappa^{\mathrm{II}}}{\kappa^{\mathrm{I}} + \kappa^{\mathrm{II}}}, \\
(R_{\mathrm{PS}})_{\mathrm{H}} &= \frac{\sin\theta}{2\cos j_{\mathrm{H}}}\left[(1 - V_{\mathrm{rsH}})\frac{\Delta\rho}{\rho} - 2V_{\mathrm{rsH}}\frac{\Delta V_{\mathrm{S}}}{V_{\mathrm{S}}}\right], \\
(R_{\mathrm{PS}})_{\mathrm{In}} &= \frac{\sin\theta}{2\cos j_{\mathrm{In}}}\left[(1 - V_{\mathrm{rsIn}})\frac{\Delta\rho}{\rho} - 2V_{\mathrm{rsIn}}\frac{\Delta V_{\mathrm{S}}}{V_{\mathrm{S}}}\right], \\
(T_{\mathrm{PS}})_{\mathrm{H}} &= \frac{\sin\theta}{2\cos j_{\mathrm{H}}}\left[(1 - V_{\mathrm{tsH}})\frac{\Delta\rho}{\rho} - 2V_{\mathrm{tsH}}\frac{\Delta V_{\mathrm{S}}}{V_{\mathrm{S}}}\right], \\
(T_{\mathrm{PS}})_{\mathrm{In}} &= \frac{\sin\theta}{2\cos j_{\mathrm{In}}}\left[(1 - V_{\mathrm{tsIn}})\frac{\Delta\rho}{\rho} - 2V_{\mathrm{tsIn}}\frac{\Delta V_{\mathrm{S}}}{V_{\mathrm{S}}}\right].
\end{aligned} \tag{19}
$$

The perturbations using equations 9, 10, and 19 can be written as

$$
\begin{aligned}
&\frac{\Delta\rho}{\rho} = \frac{2(\rho^{\mathrm{II}} - \rho^{\mathrm{I}})}{(\rho^{\mathrm{I}} + \rho^{\mathrm{II}})}, \quad \frac{\Delta V_{\mathrm{S}}}{V_{\mathrm{S}}} = \frac{2(V_{\mathrm{S}}^{\mathrm{II}} - V_{\mathrm{S}}^{\mathrm{I}})}{(V_{\mathrm{S}}^{\mathrm{I}} + V_{\mathrm{S}}^{\mathrm{II}})}, \\
&\cos j_{\mathrm{H}} = \sqrt{1 - \left(\frac{V_{\mathrm{S}}}{V_{\mathrm{H}}}\right)^2\sin^2\theta}, \\
&\cos j_{\mathrm{In}} = \sqrt{1 - \left(\frac{V_{\mathrm{S}}}{V_{\mathrm{In}}}\right)^2\sin^2\theta}, \\
&V_{\mathrm{rsH}} = 2\sin^2\theta\left(\frac{V_{\mathrm{S}}}{V_{\mathrm{H}}}\right)^2 - 2\cos\theta\cos j_{\mathrm{H}}\frac{V_{\mathrm{S}}}{V_{\mathrm{H}}}, \\
&V_{\mathrm{rsIn}} = 2\sin^2\theta\left(\frac{V_{\mathrm{S}}}{V_{\mathrm{In}}}\right)^2 - 2\cos\theta\cos j_{\mathrm{In}}\frac{V_{\mathrm{S}}}{V_{\mathrm{In}}}, \\
&V_{\mathrm{tsH}} = 2\sin^2\theta\left(\frac{V_{\mathrm{S}}}{V_{\mathrm{H}}}\right)^2 + 2\cos\theta\cos j_{\mathrm{H}}\frac{V_{\mathrm{S}}}{V_{\mathrm{H}}}, \\
&V_{\mathrm{tsIn}} = 2\sin^2\theta\left(\frac{V_{\mathrm{S}}}{V_{\mathrm{In}}}\right)^2 + 2\cos\theta\cos j_{\mathrm{In}}\frac{V_{\mathrm{S}}}{V_{\mathrm{In}}}.
\end{aligned} \tag{20}
$$

Energy-flow balance

Across a welded interface, the normal component of the time-averaged energy flux is continuous. It is the consequence of imposing the continuity of normal stress and displacement (velocity). Following Carcione (2014) and Wang et al. (2020a, 2021), we obtain the averaged energy intensity:

$$
\langle E\rangle = \frac{1}{2}\mathrm{Re}(\sigma_{zz}\cdot V_z^* + \sigma_{xz}\cdot V_x^*), \tag{21}
$$

where V_x and V_z are particle-velocity components and the superscript "*" denotes complex conjugate. The energy partition in the incidence medium associated with the four waves is

$$
\langle \mathbf{E}^{\mathrm{I}}\rangle = \frac{1}{2}\mathrm{Re}\{[\boldsymbol{\chi}]^{\mathrm{I}}\cdot[\boldsymbol{\iota}^*]^{\mathrm{I}}\}, \tag{22}
$$

where

$$
\begin{aligned}
&[\chi_{m1}]^{\mathrm{I}} = \sigma_{zz}^m, \quad [\chi_{m2}]^{\mathrm{I}} = \sigma_{xz}^m, \\
&[\iota_{2m}]^{\mathrm{I}} = V_x^m, \quad m = (0,1,2,3),
\end{aligned} \tag{23}
$$

where the square matrix of order four (E_{mn}, $m,n = 0,1,2,3$) is introduced to describe the energy fluxes and the diagonal entries corresponding to the incident (E_{00}^{I}), reflected P (E_{11}^{I}), T (E_{22}^{I}), and S (E_{33}^{I}) waves, respectively, whose interactions are represented by the off-diagonal elements.

Moreover, it can be shown that the energy flux in the transmission medium is

$$
\langle \mathbf{E}^{\mathrm{II}}\rangle = \frac{1}{2}\mathrm{Re}\{[\boldsymbol{\chi}]^{\mathrm{II}}\cdot[\boldsymbol{\iota}^*]^{\mathrm{II}}\}. \tag{24}
$$

The expressions of $[\boldsymbol{\chi}]^{\mathrm{II}}$ and $[\boldsymbol{\iota}]^{\mathrm{II}}$ are analogous to those of equation 23, where here $m = 4,5,6$. Matrix $\langle \mathbf{E}^{\mathrm{II}}\rangle$ is of third order related to the three waves in medium Ω_{II}: E_{44}^{II}, E_{55}^{II}, and E_{66}^{II} associated with the transmitted P, T, and S waves, respectively.

Energy ratios (ERs) can be obtained as the energy flux divided by E_{00}^{I}:

$$
\begin{aligned}
\mathrm{ER}_{\mathrm{sum}} &= \left[\sum_{m=1}^{3}\left(\frac{\langle E_{m0}^{\mathrm{I}}\rangle}{\langle E_{00}^{\mathrm{I}}\rangle} + \frac{\langle E_{0m}^{\mathrm{I}}\rangle}{\langle E_{00}^{\mathrm{I}}\rangle} + \sum_{n=1}^{3}\frac{\langle E_{mn}^{\mathrm{I}}\rangle}{\langle E_{00}^{\mathrm{I}}\rangle}\right)\right] \\
&\quad - \left[\sum_{m=4}^{6}\sum_{n=4}^{6}\frac{\langle E_{mn}^{\mathrm{II}}\rangle}{\langle E_{00}^{\mathrm{I}}\rangle}\right] = -1,
\end{aligned} \tag{25}
$$

and the interference energy ratio ($\mathrm{ER}_{\mathrm{in}}$) is the sum of the interactions between the incident wave and the reflected waves ($\mathrm{ER}_{\mathrm{r}}^{\mathrm{I}}$) and the interactions among the transmitted waves ($\mathrm{ER}_{\mathrm{t}}^{\mathrm{II}}$):

$$
\mathrm{ER}_{\mathrm{in}} = \mathrm{ER}_{\mathrm{r}}^{\mathrm{I}} + \mathrm{ER}_{\mathrm{t}}^{\mathrm{II}}, \tag{26}
$$

where

$$
\begin{aligned}
\mathrm{ER}_{\mathrm{r}}^{\mathrm{I}} &= \sum_{m=0}^{3}\left(\sum_{n=0}^{3}\frac{\langle E_{mn}^{\mathrm{I}}\rangle}{\langle E_{00}^{\mathrm{I}}\rangle} - \frac{\langle E_{mm}^{\mathrm{I}}\rangle}{\langle E_{00}^{\mathrm{I}}\rangle}\right), \\
\mathrm{ER}_{\mathrm{t}}^{\mathrm{II}} &= \sum_{m=4}^{6}\left(\sum_{n=4}^{6}\frac{\langle E_{mn}^{\mathrm{II}}\rangle}{\langle E_{00}^{\mathrm{I}}\rangle} - \frac{\langle E_{mm}^{\mathrm{II}}\rangle}{\langle E_{00}^{\mathrm{I}}\rangle}\right).
\end{aligned} \tag{27}
$$

EXAMPLES

We consider the thermoelastic material properties given in Table 1, which are taken from Schon (2011). These values yield the relaxation time (τ), according to Carcione et al. (2019):

$$
\begin{aligned}
\tau^{\mathrm{I}} &= \frac{\bar{\gamma}^{\mathrm{I}}}{c^{\mathrm{I}}(V_0^{\mathrm{I}})^2} = 0.23\ \mathrm{ns}, \\
\tau^{\mathrm{II}} &= \frac{\bar{\gamma}^{\mathrm{II}}}{c^{\mathrm{II}}(V_0^{\mathrm{II}})^2} = 0.21\ \mathrm{ns}.
\end{aligned} \tag{28}
$$

Downloaded 11/13/23 to 140.105.71.236. Redistribution subject to SEG license or copyright; see Terms of Use at http://library.seg.org/page/policies/terms
DOI:10.1190/geo2021-0815.1

Attenuation is caused by the thermal effects, implying complex wavenumbers, which depend on the inhomogeneity angle γ. Figure 2 shows the phase velocities and attenuation coefficients of the P and T waves as a function of frequency in the incidence (^{I}) and transmission (^{II}) media where $\gamma_0 = 0°$, 40°, and 80° are assumed. As can be seen, increasing γ_0 the dispersion increases at high frequencies because the imaginary part of k in equation 7 is significant, also increasing the attenuation of the P wave (Figure 2b), according to the Kramers-Kronig relations (e.g., Carcione, 2014). The P-wave attenuation peak is approximately located at the relaxation frequency $(1/(2\pi\tau))$. At low frequencies, the phase velocity of the T wave is almost zero and the attenuation is high, indicating a diffusive behavior (Figure 2c and 2d). The effect of γ_0 can be ignored at seismic frequencies. On the other hand, the velocity and attenuation of the S waves are not affected by the thermal effects (equation 10). These consequences are true for homogeneous media, whereas in inhomogeneous media, the thermal effects may have an effect at seismic frequencies on all of the waves (e.g., Carcione et al., 2020, 2021), as shown next when we analyze the S-wave scattering coefficients.

To verify the accuracy of our approximation to the Zoeppritz equations, we compute the conservation of energy from equation 25, as in Wang et al. (2020a, Figure 7) and Wang et al. (2021, Figure 8). Next, we compare the theories of elasticity and thermoelasticity to illustrate the effects induced by the thermal properties and test the approximation. Figure 3a and 3b shows the P-wave R/T coefficients for an incident P wave with a frequency of 75 Hz, respectively. The P-wave phase velocities in the upper and lower media are 4219 m/s and 4263 m/s, respectively, according to equation 9 and Figure 2a. We observe that the elastic approximation is close to the exact solution until 70°. A Brewster angle (θ_{B}) is defined as the incidence angle for which $R_{\mathrm{PP}} = 0$ can be seen (Pujol, 2003; Carcione, 2014) (see Figure 3a). Using the first equation of equation 19, we obtain the approximations:

$$\xi \sin^4\theta_{\mathrm{B}} - \left(\xi + \frac{\Delta\rho}{\rho}\right)\sin^2\theta_{\mathrm{B}} + \frac{\Delta\rho}{\rho} + \frac{\Delta V_{\mathrm{P}}}{V_{\mathrm{P}}} = 0, \tag{29}$$

where

$$\left(\frac{\Delta V_{\mathrm{P}}}{V_{\mathrm{P}}}\right)_{\mathrm{H}} = \frac{2(V_{\mathrm{H}}^{\mathrm{II}} - V_{\mathrm{H}}^{\mathrm{I}})}{(V_{\mathrm{H}}^{\mathrm{I}} + V_{\mathrm{H}}^{\mathrm{II}})},$$
$$\left(\frac{\Delta V_{\mathrm{P}}}{V_{\mathrm{P}}}\right)_{\mathrm{In}} = \frac{2(\kappa^{\mathrm{I}} - \kappa^{\mathrm{II}})}{(\kappa^{\mathrm{I}} + \kappa^{\mathrm{II}})},$$
$$\xi = 4\left(\frac{V_{\mathrm{S}}}{V_{\mathrm{P}}}\right)^2 \frac{\Delta\rho}{\rho} + 8\left(\frac{V_{\mathrm{S}}}{V_{\mathrm{P}}}\right)^2 \frac{\Delta V_{\mathrm{S}}}{V_{\mathrm{S}}}, \tag{30}$$

and the Brewster angle is

$$\sin^2\theta_{\mathrm{B}} = \frac{1}{2\xi}\left(\left(\xi + \frac{\Delta\rho}{\rho}\right) \pm \sqrt{\left(\xi + \frac{\Delta\rho}{\rho}\right)^2 - 4\xi\left(\frac{\Delta\rho}{\rho} + \frac{\Delta V_{\mathrm{P}}}{V_{\mathrm{P}}}\right)}\right). \tag{31}$$

Angle θ_{B} is 23.06° and 71.14° in the elastic case and 17.90° and 79.33° in the thermoelastic case. From equations 17 and 18, the exact θ_{B} is 23.61° and 68.65° in the elastic case (Aki and Richards, 2002, equation 5.40_{I}) and 18.47° in the thermoelastic case, as shown in Figure 3a. Compared with gradient, due to the existence of thermal waves, the influences of thermoelastic theory on fast P wave intercept are more significant. Figure 4 compares the elastic and thermoelastic S-wave R/T coefficients with the new approximation. The P-wave coefficients are shown in Figure 5, in which the velocities and densities are those of Pilant (1979, Figure 12-3) (the critical angle is 39.70°), whose exact and approximate coefficients further illustrate the applicability of equation 19.

Figure 6 shows synthetic common-shot gathers (Figure 6a and 6b), and the respective traveltimes (Figure 6c) based on the elastic (the solid line) and thermoelastic (the dashed line) approximate equations. The synthetic seismogram is computed in the time-angle domain as a convolution between the approximate equation and a Ricker wavelet (Bourbie and Gonzalez-Serrano, 1983), whose main frequencies are 75 Hz (Figure 6a) and 25 Hz (Figure 6b). The distance between the interface and the receivers is 100 m. The amplitude variations and arrival times of the reflection events are useful to provide information about the in-situ rock properties. The amplitudes corresponding to the

Table 1. Medium properties.

Absolute temperature (K)	$T_0^{\mathrm{I}} = 330$	$T_0^{\mathrm{II}} = 350$
Density (kg/m^3)	$\rho^{\mathrm{I}} = 2425$	$\rho^{\mathrm{II}} = 2475$
Velocity ($\sqrt{(\lambda + 2\mu)/\rho}$) (m/s)	$V_0^{\mathrm{I}} = 3757$	$V_0^{\mathrm{II}} = 3898$
Velocity ($\sqrt{\mu/\rho}$) (m/s)	$V_{\mathrm{S}}^{\mathrm{I}} = 2390$	$V_{\mathrm{S}}^{\mathrm{II}} = 2666$
Specific heat (kJ/(kg · K))	$c^{\mathrm{I}} = 0.9$	$c^{\mathrm{II}} = 0.92$
Thermal conductivity (W/(m · K))	$\bar{\gamma}^{\mathrm{I}} = 2.9$	$\bar{\gamma}^{\mathrm{II}} = 3.0$
Coefficient of thermal expansion ($\times 10^{-6}$ K^{-1})	$\bar{\alpha}^{\mathrm{I}} = 3.3$	$\bar{\alpha}^{\mathrm{II}} = 3.28$

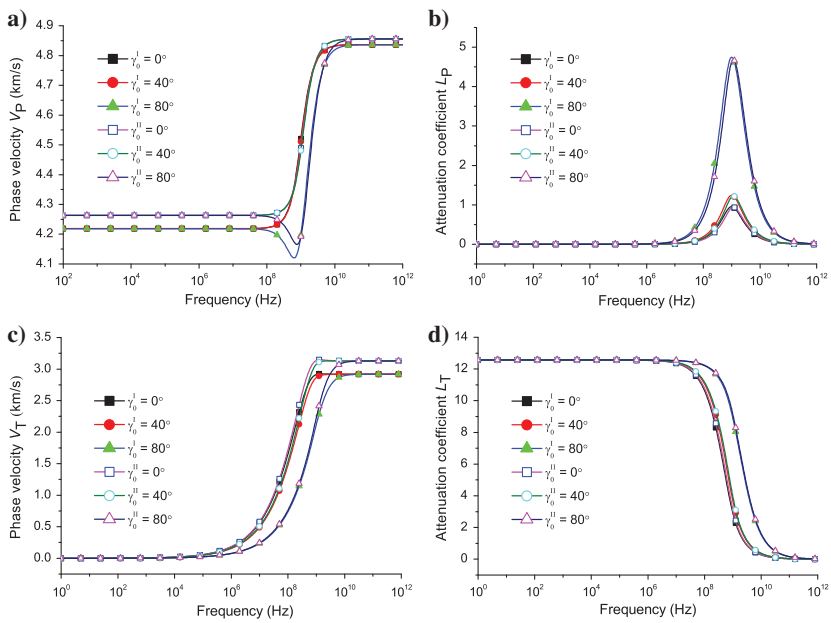

Figure 2. Phase velocities of the fast (a) P and (c) T waves as a function of frequency for the homogeneous ($\gamma_0 = 0°$) and inhomogeneous ($\gamma_0 = 40°$ and 80°) cases and (b and d) corresponding attenuation coefficients. The superscripts I and II of γ_0 correspond to the upper and lower media, respectively (Ω_{I} and Ω_{II}).

Downloaded 11/13/23 to 140.105.71.236. Redistribution subject to SEG license or copyright; see Terms of Use at http://library.seg.org/page/policies/terms
DOI:10.1190/geo2021-0815.1

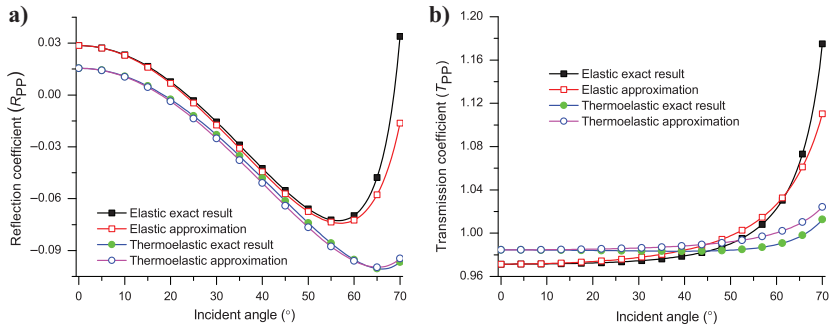

Figure 3. Comparison between the (a) reflection and (b) transmission coefficients of the P wave obtained with the exact and approximate solutions at 75 Hz.

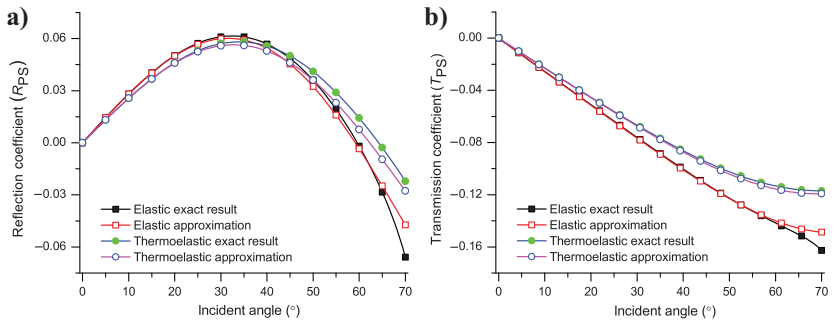

Figure 4. Comparison between the (a) reflection and (b) transmission coefficients of the S wave obtained with the exact and approximate solutions at 75 Hz.

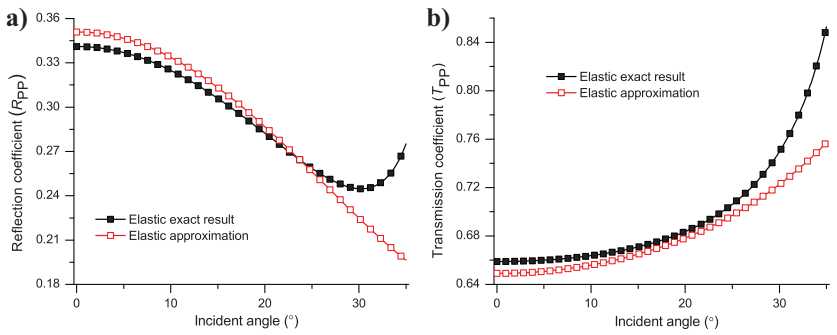

Figure 5. The exact and approximate results of the (a) reflection and (b) transmission coefficients with an incident P wave based on Pilant (1979, Figure 12-3) parameters.

elastic model are higher at small angles, but there is a phase change beyond θ_B. Deeper reservoirs correspond to lower frequencies. As the angle increases, the amplitudes first increase and then decrease, but due to the low attenuation of the seismic frequencies (Figure 2), the change is not significant. Frequency is more sensitive to pores and their filling material (Wu et al., 2015; Zhao et al., 2015), but the theory is based on elastic solids without pores, so it has little effect on the attenuation of fast longitudinal waves. The traveltimes corresponding to the thermoelastic model are smaller due to the thermal effects. Comparing Figure 6a and 6b, it can be seen that the low-frequency wave packet is significantly wider than the high-frequency counterpart, whereas frequency has little effect on the arrival times in the thermoelastic case. Therefore, the arrival time related to the phase velocity indicates that the thermal effects play a significant role, as shown in Figure 6c.

To analyze how temperature affects the amplitudes, let us consider two other models in which the transmission medium has a higher temperature (400 K and 450 K) and the thermal properties are given in Table 2 (Schon, 2011). Figure 7 compares the coefficients, showing that the magnitude of R_{PP} decreases with T_0, whereas that of T_{PP} increases, taking the reflected and transmitted P waves as a reference. Higher T_0 implies lower velocity, thus reducing the impedance contrast. This implies that more energy is transmitted and less is reflected. For small angles, a better accuracy of the approximate equation can be obtained with a higher T_0. However, there are differences at larger angles. The corresponding synthetic seismogram shown in Figure 8 is consistent with the preceding descriptions. We apply the proposed thermoelastic AVO modeling to field data from the Shuntuoguole uplift of the Tarim Basin (S area) in Northwest China (Wei et al., 2021). Figure 9a shows a seismic imaging profile in which the target reservoir with the temperature more than 410 K is marked by a dashed red line at common-depth point (CDP) 1020. The corresponding prestack

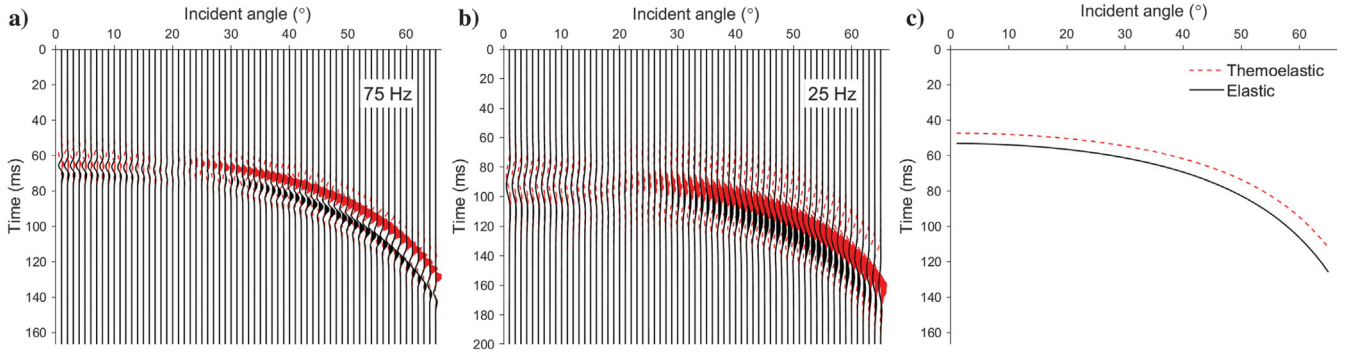

Figure 6. Synthetic seismograms of (a) 75 Hz and (b) 25 Hz and (c) traveltimes corresponding to the elastic (solid black lines) and thermoelastic approximations (dotted red lines).

Downloaded 11/13/23 to 140.105.71.236. Redistribution subject to SEG license or copyright; see Terms of Use at http://library.seg.org/page/policies/terms
DOI:10.1190/geo2021-0815.1

angular gather (migrated) is shown in Figure 9b, in which the target reservoir is indicated by a box. We extract the average values of V_0, V_S, ρ, λ, and μ from the reservoir interval of logging data, which are 4489 m/s, 2494 m/s, 2510 kg/m^3, 12 GPa, and 19 GPa, respectively. The reservoir rocks are mainly limestones with high calcite contents and a small amount of dolomite. Based on the corresponding thermal properties (Schon, 2011) of the rocks at the logging temperature, we obtain $\bar{\gamma}$ = 2.31 W/(m · K), c = 920 J/(kg · K), and $\bar{\alpha} = 3.3 \times 10^{-6}$ K^{-1}. Likewise, we obtain the average values as the upper layer parameters, which are 4331 m/s, 2406 m/s, 2467 kg/m^3, 11 GPa, 17.7 GPa, 2.3 W/(m · K), 919.8 J/(kg · K), and 3.3×10^{-6} K^{-1}, respectively. It should be stressed that the thermoelastic AVO theory presented in this study is limited to solid media, implying that temperature only

Table 2. High-temperature medium properties.

$(T_0^{\mathrm{II}})_1 = 400$ K	$(T_0^{\mathrm{II}})_2 = 450$ K
$(\rho^{\mathrm{II}})_1 = 2465$ kg/m^3	$(\rho^{\mathrm{II}})_2 = 2455$ kg/m^3
$(V_0^{\mathrm{II}})_1 = 3858$ m/s	$(V_0^{\mathrm{II}})_2 = 3800$ m/s
$(V_S^{\mathrm{II}})_1 = 2600$ m/s	$(V_S^{\mathrm{II}})_2 = 2530$ m/s
$(c^{\mathrm{II}})_1 = 0.96$ kJ/(kg · K)	$(c^{\mathrm{II}})_2 = 0.98$ kJ/(kg · K)
$(\bar{\gamma}^{\mathrm{II}})_1 = 3.2$ W/(m · K)	$(\bar{\gamma}^{\mathrm{II}})_2 = 3.3$ W/(m · K)
$(\bar{\alpha}^{\mathrm{II}})_1 = 3.25 \times 10^{-6}$ K^{-1}	$(\bar{\alpha}^{\mathrm{II}})_2 = 3.23 \times 10^{-6}$ K^{-1}

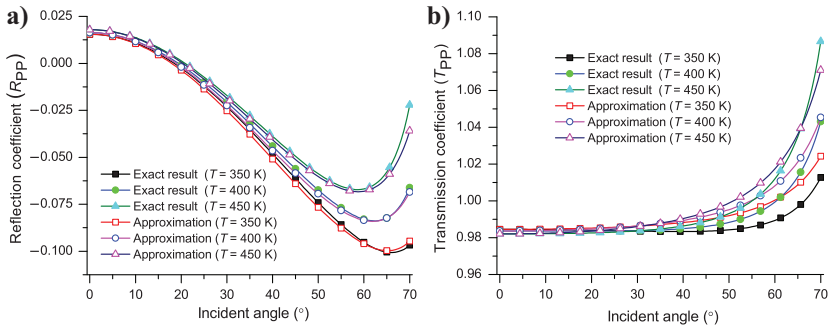

Figure 7. (a) Reflection and (b) transmission coefficients of the P wave obtained with the AVO approximation at 75 Hz with different absolute temperatures of the lower (transmission) medium. The medium properties are shown in Table 2.

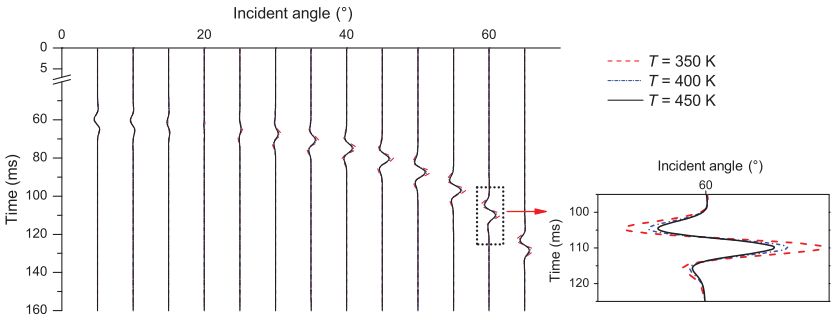

Figure 8. Synthetic seismograms for different absolute temperatures of the lower (transmission) medium.

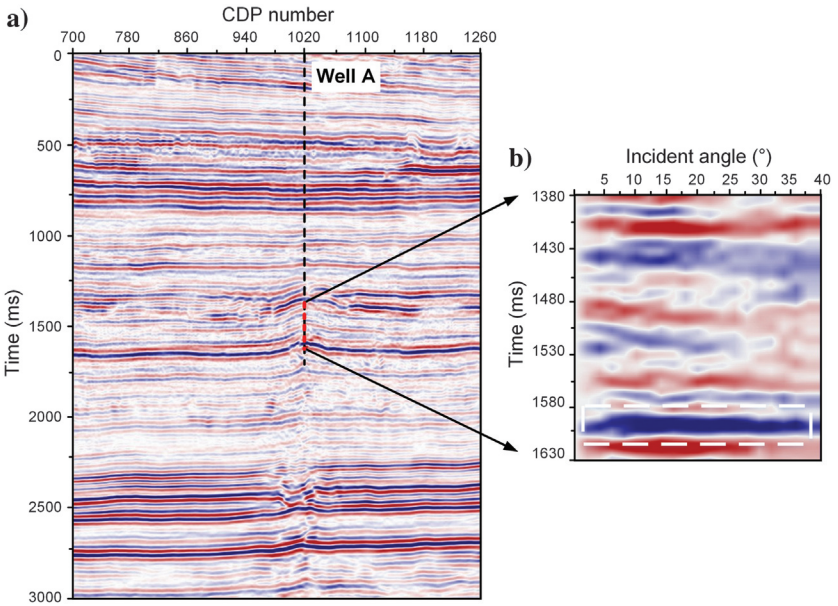

Figure 9. (a) A seismic imaging profile from the S area in Northwest China, where the target reservoir with the temperature more than 410 K is marked by a dashed red line at CDP 1020. (b) The corresponding prestack angular gather (migrated) with the target reservoir is indicated by a box.

Downloaded 11/13/23 to 140.105.71.236. Redistribution subject to SEG license or copyright; see Terms of Use at http://library.seg.org/page/policies/terms
DOI:10.1190/geo2021-0815.1

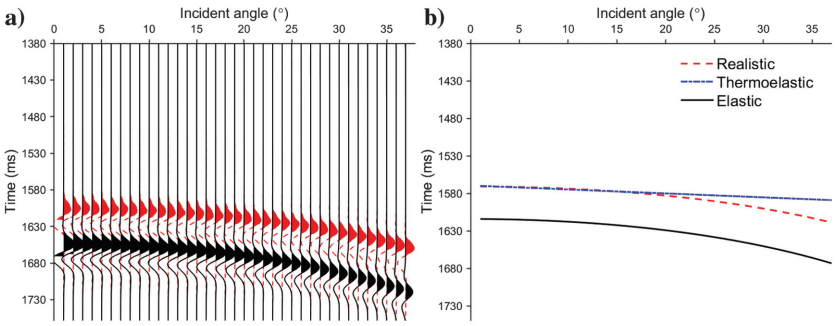

Figure 10. (a) Synthetic angular gather (unmigrated) based on the traditional elastic AVO (black wiggles) and thermoelastic AVO (red wiggles), respectively. The synthetic seismograms are drawn together in an angular gather for the sake of comparison. (b) Comparison of angle-dependent traveltimes among the elastic AVO (the solid black line), thermoelastic AVO (the dashed red line), and realistic angular gather (the dotted blue line). The reason for the time difference at large angles between the dotted blue and dashed red lines is that the realistic angular gather shown in Figure 9b is migrated.

affects velocity instead of attenuation. Therefore, we focus on the comparison in traveltime between the realistic and synthetic gathers. Figure 10a shows the synthetic angular gather (unmigrated) based on the traditional elastic AVO (black wiggles) and thermoelastic AVO (red wiggles), respectively. We see that the thermoelastic AVO synthetic gather yields more accurate traveltimes at small angles in terms of Figure 10a. To further demonstrate the traveltime difference between elastic and thermoelastic AVO synthetic gathers, we pick up the angle-dependent traveltimes of these gathers and compare with the actual traveltime from Figure 9b. As shown in Figure 10b, the elastic AVO shows a relatively large error from the actual traveltime, whereas the time difference at large angles between the thermoelastic AVO synthetic and actual angular gathers is due to the fact that the latter available to us is migrated, as shown in Figure 9b. The proposed thermoelastic AVO is confined to solid media, in which the effect of porosities and associated fluids are not considered. Considering the sensitivity of pore fluids to temperature, it is necessary to extend the thermoelastic AVO to poroelastic media for practical applications.

CONCLUSION

We analyze AVO based on the thermoelastic approximation for an interface separating two thermoelastic media for an incident P wave, based on the LS theory. The scattering coefficients are computed by taking into account the presence of inhomogeneous plane waves and six boundary conditions (generalized Snell law) and verified with the conservation of energy. Then, we compute synthetic seismograms and arrival times corresponding to the thermoelasticity and elasticity models for a specific case. We observe a phase reversal at a Brewster angle, stronger in the thermoelastic case. We also consider two models with higher absolute temperatures at the transmission medium, showing that the scattering coefficients are affected by this temperature. Data taken from a real CDP gather serve to build a model and verify the accuracy of the AVO approximation considering the thermal effects.

ACKNOWLEDGMENTS

The research is supported by the National Natural Science Foundation of China (grant no. 41821002), 111 project "Deep-Superdeep Oil & Gas Geophysical Exploration" (B18055), and Innovation fund project for a graduate student of China University of Petroleum (East China), supported by "the Fundamental Research Funds for the Central Universities" (22CX04017A).

DATA AND MATERIALS AVAILABILITY

Data associated with this research are available and can be obtained by contacting the corresponding author.

APPENDIX A

CALCULATION FOR COMPLEX WAVENUMBER

Substituting the Helmholtz decomposition (equation 4) into thermoelasticity equations 1 and 3, we obtain

$$\begin{aligned}&(\lambda+2\mu)\nabla^2\phi-\beta T=\rho\ddot{\phi},\\&\beta T_0(\nabla^2\dot{\phi}+\tau\nabla^2\ddot{\phi})=\bar{\gamma}\nabla^2 T-c(\dot{T}+\tau\ddot{T}),\\&\mu\nabla^2\psi-\rho\ddot{\psi}=0,\end{aligned}\tag{A-1}$$

where ∇^2 is the Laplacian operator. Using the plane waves and complex wavenumber vector (equations 5 and 6), the equation is

$$\mathbf{M}\cdot\mathbf{A}=\begin{bmatrix}\beta & k^2(\lambda+2\mu)-\rho\omega^2\\ \bar{\gamma}k^2+\omega c(\mathrm{i}-\tau\omega) & k^2\beta T_0\omega(\tau\omega-\mathrm{i})\end{bmatrix}\begin{bmatrix}A_T\\A_\phi\end{bmatrix}=0,\tag{A-2}$$

where the determinant of $\mathbf{M}$ is zero to obtain the complex wavenumber.

APPENDIX B

EXPRESSIONS FOR MATRICES B AND D

The elements of matrix $\mathbf{B}$ are given by

$$\begin{aligned}&B_{11}=p_0,\ B_{12}=p_0,\ B_{13}=-q_3,\ B_{14}=-p_0,\ B_{15}=-p_0,\ B_{16}=-q_6,\\&B_{21}=q_0,\ B_{22}=q_2,\ B_{23}=p_0,\ B_{24}=q_4,\ B_{25}=q_5,\ B_{26}=-p_0,\\&B_{31}=\rho^{\mathrm{I}}\omega^2-2\mu^{\mathrm{I}}p_0^2,\ B_{32}=\rho^{\mathrm{I}}\omega^2-2\mu^{\mathrm{I}}p_0^2,\ B_{33}=2\mu^{\mathrm{I}}p_3q_3,\ B_{34}=-(\rho^{\mathrm{II}}\omega^2-2\mu^{\mathrm{II}}p_4^2),\\&B_{35}=-(\rho^{\mathrm{II}}\omega^2-2\mu^{\mathrm{II}}p_5^2),\ B_{36}=2\mu^{\mathrm{II}}p_6q_6,\\&B_{41}=2p_0q_0,\ B_{42}=2p_2q_2,\ B_{43}=-(q_3^2-p_3^2),\ B_{44}=2\frac{\mu^{\mathrm{II}}}{\mu^{\mathrm{I}}}p_4q_4,\\&B_{45}=2\frac{\mu^{\mathrm{II}}}{\mu^{\mathrm{I}}}p_5q_5,\ B_{46}=\frac{\mu^{\mathrm{II}}}{\mu^{\mathrm{I}}}(q_6^2-p_6^2),\\&B_{51}=q_0[(\lambda^{\mathrm{I}}+2\mu^{\mathrm{I}})(p_0^2+q_0^2)-\rho^{\mathrm{I}}\omega^2],\ B_{52}=q_2[(\lambda^{\mathrm{I}}+2\mu^{\mathrm{I}})(p_2^2+q_2^2)-\rho^{\mathrm{I}}\omega^2],\\&B_{53}=0,B_{54}=\frac{\bar{\gamma}^{\mathrm{II}}\beta^{\mathrm{I}}}{\bar{\gamma}^{\mathrm{I}}\beta^{\mathrm{II}}}q_4[(\lambda^{\mathrm{II}}+2\mu^{\mathrm{II}})(p_4^2+q_4^2)-\rho^{\mathrm{II}}\omega^2],\\&B_{55}=\frac{\bar{\gamma}^{\mathrm{II}}\beta^{\mathrm{I}}}{\bar{\gamma}^{\mathrm{I}}\beta^{\mathrm{II}}}q_5[(\lambda^{\mathrm{II}}+2\mu^{\mathrm{II}})(p_5^2+q_5^2)-\rho^{\mathrm{II}}\omega^2],\ B_{56}=0,\\&B_{61}=(\lambda^{\mathrm{I}}+2\mu^{\mathrm{I}})(p_0^2+q_0^2)-\rho^{\mathrm{I}}\omega^2,\ B_{62}=(\lambda^{\mathrm{I}}+2\mu^{\mathrm{I}})(p_2^2+q_2^2)-\rho^{\mathrm{I}}\omega^2,\\&B_{63}=0,B_{64}=-\frac{\beta^{\mathrm{I}}}{\beta^{\mathrm{II}}}[(\lambda^{\mathrm{II}}+2\mu^{\mathrm{II}})(p_4^2+q_4^2)-\rho^{\mathrm{II}}\omega^2],\\&B_{65}=-\frac{\beta^{\mathrm{I}}}{\beta^{\mathrm{II}}}[(\lambda^{\mathrm{II}}+2\mu^{\mathrm{II}})(p_5^2+q_5^2)-\rho^{\mathrm{II}}\omega^2],\ B_{66}=0.\end{aligned}\tag{B-1}$$

Downloaded 11/13/23 to 140.105.71.236. Redistribution subject to SEG license or copyright; see Terms of Use at http://library.seg.org/page/policies/terms
DOI:10.1190/geo2021-0815.1

Matrix **D** has the components:

$$
\begin{aligned}
D_{17} &= -p_0,\\
D_{27} &= q_0,\\
D_{37} &= -(\rho^{\mathrm{I}}\omega^2 - 2\mu^{\mathrm{I}}p_0^2),\\
D_{47} &= 2p_0q_0,\\
D_{57} &= q_0[(\lambda^{\mathrm{I}} + 2\mu^{\mathrm{I}})(p_0^2 + q_0^2) - \rho^{\mathrm{I}}\omega^2],\\
D_{67} &= -[(\lambda^{\mathrm{I}} + 2\mu^{\mathrm{I}})(p_0^2 + q_0^2) - \rho^{\mathrm{I}}\omega^2]. \qquad \text{(B-2)}
\end{aligned}
$$

REFERENCES

Abbas, I. A., and M. I. A. Othman, 2012, Plane waves in generalized thermo-microstretch elastic solid with thermal relaxation using finite element method: International Journal of Thermophysics, **33**, 2407–2423, doi: 10.1007/s10765-012-1340-8.

Ackerman, C. C., B. Bertman, H. A. Fairbank, and R. A. Guyer, 1966, Second sound in solid helium: Physical Review Letters, **16**, 789–791, doi: 10.1103/PhysRevLett.16.789.

Aki, K., and P. G. Richards, 2002, Quantitative seismology, 2nd ed.: University Science Books.

Batzle, M. L., D. H. Han, and R. Hofmann, 2006, Fluid mobility and frequency-dependent seismic velocity-direct measurement: Geophysics, **71**, no. 1, N1–N9, doi: 10.1190/1.2159053.

Biot, M. A., 1956a, Thermoelasticity and irreversible thermodynamics: Journal of Applied Physics, **27**, 240–253, doi: 10.1063/1.1722351.

Biot, M. A., 1956b, Theory of propagation of elastic waves in a fluid-saturated porous solid. I. Low frequency range: Journal of Acoustical Society of America, **28**, 168–178, doi: 10.1121/1.1908239.

Borcherdt, R. D., 2009, Viscoelastic waves in layered media: Cambridge University Press.

Bortfeld, R., 1961, Approximation to the reflection and transmission coefficients of plane longitudinal and transverse waves: Geophysical Prospecting, **9**, 485–502, doi: 10.1111/j.1365-2478.1961.tb01670.x.

Bourbie, T., and A. Gonzalez-Serrano, 1983, Synthetic seismograms in attenuating media: Geophysics, **48**, 1575–1587, doi: 10.1190/1.1441440.

Carcione, J. M., 1995, Constitutive model and wave equations for linear, viscoelastic, anisotropic media: Geophysics, **60**, 537–548, doi: 10.1190/1.1443791.

Carcione, J. M., 1997, Reflection and transmission of qP-qS plane waves at a plane boundary between viscoelastic transversely isotropic media: Geophysical Journal International, **129**, 669–680, doi: 10.1111/j.1365-246X.1997.tb04502.x.

Carcione, J. M., 2014, Wave fields in real media. Theory and numerical simulation of wave propagation in anisotropic, anelastic and porous media, 3rd ed.: Elsevier, 262.

Carcione, J. M., D. Gei, J. E. Santos, L. Y. Fu, and J. Ba, 2020, Canonical analytical solutions of wave-induced thermoelastic attenuation: Geophysical Journal International, **221**, 835–842, doi: 10.1093/gji/ggaa033.

Carcione, J. M., S. Picotti, and J. Ba, 2021, P- and S-wave simulation using a Cole-Cole model to incorporate thermoelastic attenuation and dispersion: The Journal of the Acoustical Society of America, **149**, 1946–1954, doi: 10.1121/10.0003749.

Carcione, J. M., Z. W. Wang, W. Ling, E. Salusti, J. Ba, and L. Y. Fu, 2019, Simulation of wave propagation in linear thermoelastic media: Geophysics, **84**, no. 1, T1–T11, doi: 10.1190/geo2018-0448.1.

Chapman, M., E. Liu, and X. Y. Li, 2006, The influence of fluid sensitive dispersion and attenuation on AVO analysis: Geophysical Journal International, **167**, 89–105, doi: 10.1111/j.1365-246X.2006.02919.x.

Deresiewicz, H., 1957, Plane waves in a thermoelastic solid: The Journal of the Acoustical Society of America, **29**, 204–209, doi: 10.1121/1.1908832.

Green, A. E., and K. A. Lindsay, 1972, Thermoelasticity: Journal of Elasticity, **2**, 1–7, doi: 10.1007/BF00045689.

Hou, W., L. Y. Fu, J. M. Carcione, and T. C. Han, 2022, Reflection and transmission of inhomogeneous plane waves in thermoelastic media: Frontiers in Earth Science, **10**, 1–16, doi: 10.3389/feart.2022.850331.

Hou, W., L. Y. Fu, J. M. Carcione, Z. W. Wang, and J. Wei, 2021b, Simulation of thermoelastic waves based on the Lord-Shulman theory: Geophysics, **86**, no. 3, T155–T164, doi: 10.1190/geo2020-0515.1.

Hou, W., L. Y. Fu, J. Wei, and Z. W. Wang, 2021a, Characteristics of wave propagation in thermoelastic medium: Chinese Journal of Geophysics (in Chinese), **64**, 1364–1374.

Ignaczak, J., and M. Ostoja-Starzewski, 2010, Thermoelasticity with finite wave speeds: Oxford Science Publications.

Jackson, H. E., C. T. Walker, and T. F. McNelly, 1970, Second sound in NaF: Physical Review Letters, **25**, 26–28, doi: 10.1103/PhysRevLett.25.26.

Koefoed, O., 1955, On the effect of Poisson's ratios of rock strata on the reflection coefficients of plane waves: Geophysical Prospecting, **3**, 381–387, doi: 10.1111/j.1365-2478.1955.tb01383.x.

Lord, H. W., and Y. Shulman, 1967, A generalized dynamical theory of thermoelasticity: Journal of the Mechanics and Physics of Solids, **15**, 299–309, doi: 10.1016/0022-5096(67)90024-5.

Maxwell, J. C., 1867, On the dynamic theory of gases: Philosophical Transactions of the Royal Society of London, **157**, 49–88, doi: 10.1098/rstl.1867.0004.

McNelly, T. F., S. J. Rogers, D. J. Channin, R. J. Rollefson, W. M. Goubau, G. E. Schmidt, J. A. Krumhansl, and R. O. Pohl, 1970, Heat pulses in NaF: Onset of second sound: Physical Review Letters, **24**, 100–102, doi: 10.1103/PhysRevLett.24.100.

Pilant, W. L., 1979, Elastic waves in the earth: Elsevier Science Publishing Company.

Pujol, J., 2003, Elastic wave propagation and generation in seismology: Cambridge University Press, 142.

Sarkar, N., and S. Mondal, 2020, Thermoelastic plane waves under the modified Green-Lindsay model with two-temperature formulation: Journal of Applied Mathematics and Mechanics/Zeitschrift für Angewandte Mathematik und Mechanik, **100**, 1–17, doi: 10.1002/zamm.201900267.

Schon, J. H., 2011, Physical properties of rocks: A workbook: Elsevier.

Sharma, M. D., 2018, Reflection-refraction of attenuated waves at the interface between a thermo-poroelastic medium and a thermoelastic medium: Waves in Random and Complex Media, **28**, 570–587, doi: 10.1080/17455030.2017.1370154.

Shen, Z., and X. Wang, 2013, The approximation of P waves reflection and transmission coefficient in viscoelastic medium and comparative analysis: Progress in Geophysics, **28**, 257–264, doi: 10.6038/pg20130127.

Shuey, R. T., 1985, A simplification of the Zoeppritz equations: Geophysics, **50**, 609–614, doi: 10.1190/1.1441936.

Singh, B., 2000, Reflection of plane sound wave from a micropolar generalized thermoelastic solid half-space: Journal of Sound and Vibration, **235**, 685–696, doi: 10.1006/jsvi.2000.2949.

Sinha, S. B., and K. A. Elsibai, 1996, Reflection of thermoelastic waves at a solid half-space with two relaxation times: Journal of Thermal Stresses, **19**, 749–762, doi: 10.1080/01495739608946205.

Wang, E., J. M. Carcione, J. Ba, and Y. Liu, 2020a, Reflection and transmission of plane elastic waves at an interface between two double-porosity media: Effect of local fluid flow: Surveys in Geophysics, **41**, 283–322, doi: 10.1007/s10712-019-09572-6.

Wang, E., J. M. Carcione, Y. Yuan, and J. Ba, 2021, Reflection of inhomogeneous plane waves at the surface of a thermo-poroelastic medium: Geophysical Journal International, **224**, 1621–1639, doi: 10.1093/gji/ggaa543.

Wang, Z. W., L. Y. Fu, J. Wei, W. Hou, J. Ba, and J. M. Carcione, 2020b, On the Green function of the Lord-Shulman thermoelasticity equations: Geophysical Journal International, **220**, 393–403, doi: 10.1093/gji/ggz453.

Wei, J., L. Y. Fu, Z. W. Wang, J. Ba, and J. M. Carcione, 2020, Green function of the Lord-Shulman thermo-poroelasticity theory: Geophysical Journal International, **221**, 1765–1776, doi: 10.1093/gji/ggaa100.

Wei, Y., J. Ba, J. M. Carcione, L. Y. Fu, and H. Qi, 2021, Temperature, differential-pressure and porosity inversion for ultra-deep carbonate reservoirs based on 3D rock physics templates: Geophysics, **86**, no. 3, M77–M89, doi: 10.1190/geo2020-0550.1.

Wu, X., M. Chapman, and E. Angerer, 2015, Interpretation of phase reversals in seismic reflections from attenuating targets: Geophysical Journal International, **200**, 690–697, doi: 10.1093/gji/ggu426.

Zenkour, A. M., D. S. Mashat, and A. E. Abouelregal, 2013, The effect of dual-phase-lag model on reflection of thermoelastic waves in a solid half space with variable material properties: Acta Mechanica Solida Sinica, **26**, 659–670, doi: 10.1016/S0894-9166(14)60009-4.

Zhao, L., D. H. Han, Q. Yao, R. Zhou, and F. Yan, 2015, Seismic reflection dispersion due to wave-induced fluid flow in heterogeneous reservoir rocks: Geophysics, **80**, no. 3, D221–D235, doi: 10.1190/geo2014-0307.1.

Zhao, L., H. Yuan, J. Yang, D. H. Han, J. Geng, R. Zhou, H. Li, and Q. Yao, 2017, Mobility effect on poroelastic seismic signatures in partially saturated rocks with applications in time-lapse monitoring of a heavy oil reservoir: Journal of Geophysical Research: Solid Earth, **122**, 8872–8891, doi: 10.1002/2017JB014303.

Zoeppritz, K., 1919, Erdbebenwellen VIII B, Uber die reflexion und durchgang seismischer wellen durch Unstetigkeitsflachen: Nachrichten von der Gesellschaft der Wissenschaften zu Göttingen, Mathematisch-Physikalische Klasse, **1919**, 66–84.

Zong, Z., X. Yin, and G. Wu, 2012, AVO inversion and poroelasticity with P- and S-wave moduli: Geophysics, **77**, no. 6, N17–N24, doi: 10.1190/geo2011-0214.1.

Biographies and photographs of the authors are not available.